ACS APPLIED MATERIALS & INTERFACES

Research Article

www.acsami.org

Novel Preparation of Anatase TiO_2@Reduced Graphene Oxide Hybrids for High-Performance Dye-Sensitized Solar Cells

Gang Cheng,[†] M. Shaheer Akhtar,[†,‡] O-Bong Yang,[†] and Florian J. Stadler*[,†]

[†]School of Semiconductor and Chemical Engineering, Chonbuk National University, 567 Baekjedaero, Deokjin-gu, Jeonju, Jeonbuk 561-756, Republic of Korea

[‡]New and Renewable Energy Materials Development Center (NewREC), Chonbuk National University, Jeonbuk, Republic of Korea

Supporting Information

ABSTRACT: An effective method was developed to prepare hybrid materials of TiO_2 nanoparticles on reduced graphene oxide (RGO) sheets for application in solar cells. The morphology, size, and crystal phase of the TiO_2 nanoparticles and TiO_2@reduced graphene oxide (TiO_2@RGO) hybrids were investigated in detail by X-ray diffraction (XRD), scanning electron microscopy (SEM), transmission electron microscopy (TEM), selected area electron diffraction (SAED), X-ray photoelectron spectroscopy (XPS), Raman, and UV-vis diffuse reflectance spectroscopy. A possible growth mechanism of TiO_2@RGO hybrids is proposed based on observations of the TiO_2 nanoparticles obtained from the hydrolysis process under different conditions. The effects of different reduced graphene oxide contents on the energy conversion efficiency of the dye-sensitized solar cells (DSSCs) based on *J*−*V* and incident photon-to-current conversion efficiency (IPCE) spectra are also discussed. DSSCs based on TiO_2@RGO hybrid photoanodes with a graphene content of 1.6 wt % showed an overall light-to-electricity conversion efficiency of 7.68%, which is much higher than that of pure anatase nanoparticles (4.78%) accompanied by a short-circuit current density of 18.39 mA cm^2, an open-circuit voltage of 0.682 V, and a fill factor of 61.2%.

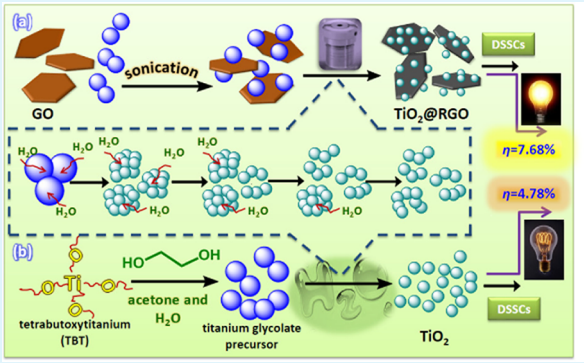

KEYWORDS: *TiO_2 nanoparticles, reduced graphene oxide, hybrid materials, dye-sensitized solar cells, hydrothermal synthesis, two-step solution-phase approach*

1. INTRODUCTION

Graphene, a single-layer, two-dimensional sheet of sp^2-bonded carbon atoms, possesses outstanding mechanical, thermal, optical, and electrical properties.[1] The large-scale, reliable production of graphene derivatives mainly including graphene oxide (GO) and reduced graphene oxide (RGO) provides possibilities to synthesize a wide variety of graphene-involved functional materials for use in a varity of applications.[2,3] Therefore, graphene has attracted considerable attention and research interest in recent years in the fields of materials for applications in energy conversion and storage,[4−7] photoelectronic devices,[8−10] photocatalysts,[11−14] polymer composites,[15,16] and ultra-strong sheet-like materials.[17,18]

TiO_2-based dye-sensitized solar cells (DSSCs) offer one of the most promising alternatives to sustainable, clean, and renewable energy for transferring inexhaustible sunlight into electricity, as they possess advantages such as low cost and environmental friendliness, and they can, in principle, be produced on a large scale.[19,20] However, electron transport in disordered TiO_2 nanoparticles with a random transit path enhances the possibility of charger recombination and thus reduces the photocurrent and the performance of the device.[21,22] Thus, designing a photoanode with a fast transport pathway from the photoinjected carriers to the electrically conductive electrode would remarkably improve the performance of DSSCs.[23−25] To enhance electron transport and reduce recombination, several kinds of photoanode materials have been employed in the past decade, including doped TiO_2,[26,27] metal/metal oxide−TiO_2 hybrid, composite and core−shell structures,[28−30] porous TiO_2 structures,[31−35] and TiO_2−carbon materials.[36−38]

Graphene possesses high electronic conductivity, huge specific surface areas, great mechanical strength, and chemical stability and can behave as an electron transfer support for increasing the power conversion efficiency of DSSCs.[39,40] Recently, much attention has been devoted to prepare TiO_2@reduced graphene oxide for photoanode materials in DSSCs. Various TiO_2@reduced graphene oxide composites with tunable TiO_2 nanostructures (e.g., nanoparticles, nanorods, nanofibers, and nanospheres) have been fabricated via various synthetic routes including solvothermal,[41] microwave-assisted,[42] electrospinning,[13,43] chemical exfoliation,[40] and photocatalytic processes.[7] Although well-defined nanostructures of TiO_2@reduced graphene oxide composites have been

Received: April 12, 2013
Accepted: June 18, 2013
Published: June 18, 2013

fabricated, it still remains a challenge to develop an alternative route to fabricate such composites with good attachment of TiO_2 nanoparticles and improved properties.

In this work, we developed a two-step wet-chemical approach to synthesize TiO_2@reduced graphene oxide (TiO_2@RGO) hybrid materials for solar energy conversion applications. On the basis of electron microscopy observations of the TiO_2 products obtained under different reaction times, a possible growth mechanism of the TiO_2@RGO hybrids involving an in situ hydrolysis process was proposed. The fabricated dye-sensitized solar cells with the TiO_2@RGO hybrid photoanode showed a superior conversion efficiency of 7.68% compared to the performance of the bare TiO_2 nanoparticle photoanode (4.78%).

2. EXPERIMENTAL SECTION

Materials Synthesis. All of the chemicals with analytical grade were used directly, and deionized (DI) water was used for all sample preparations.

The titanium glycolate precursor was fabricated according to a previously reported method which was altered with major modifications.[44,45] In a typical synthesis, a proper amount of tetrabutoxytitanium was added to 50 mL of ethylene glycol and magnetically stirred for 2 h at 60 °C in a water bath. After cooling to room temperature, the transparent solution was poured into a mixed solution of acetone and deionized water (v/v = 5:1) with vigorous stirring. The precipitate immediately occurred, and the suspension was further stirred for 1.5 h. After that, the solid products were collected by centrifugation and washed with deionized ethanol and water six times and were finally dried overnight at 60 °C.

Graphene oxide (GO) was fabricated from natural graphite powders via a Hummers' method with major modifications.[46−48] In a typical synthesis, the mixture containing 2.0 g of graphite powders and 46 mL of H_2SO_4 (98%) was first placed in an ice water bath. Next, 6.0 g of $KMnO_4$ was added lowly into the mixed suspension within 40 min under vigorous stirring for 2 h while maintaining the temperature in the range of 0−5 °C. After that, deep-green mixtures were obtained and then transferred in an oil bath at 35 ± 2 °C with stirring for 2 h. Subsequently, 92 mL of de-ionized water was slowly added into the above mixtures, and the reaction system was further stirred for 1 h. The obtained mixtures were then poured into 280 mL of deionized water under vigorous stirring. Finally, 35% H_2O_2 was added to the reaction mixtures to remove the remaining $KMnO_4$. The color of the products changed to bright yellow, confirming the transformation of graphite oxide from graphite. Meanwhile, a dilute HCl solution (1 M) was prepared from 37% HCl and distilled water. The bright yellow products obtained were subsequently washed with the prepared dilute HCl and lots of deionized water, until the pH value of the mixed suspension was ≈7. The mixtures were finally dried at 50 °C for 3 days in a vacuum oven. The vacuum-dried graphite oxide paper-like flakes were ground into a fine powder and sealed tightly in ampules for storage.

Anatase TiO_2 nanoparticle-decorated reduced graphene oxide (TiO_2@RGO) hybrids were fabricated by a hydrothermal method. Typically, different amounts of the synthesized GO and 0.1 g of the as-synthesized titanium glycolate precursor were dispersed in 30 mL of deionized water under vigorous sonication. The weight ratios of GO with respect to the titanium glycolate precursor were 0, 0.8%, 1.6%, 4%, and 16%, which are referred as GT0, GT0.8, GT1.6, GT4, and GT16, respectively. Next, the homogeneous solution was transferred into a 50 mL Teflon-lined autoclave and maintained at the temperature of 180 °C for 6 h. After cooling to room temperature, the TiO_2@RGO hybrids were collected by centrifugation and washed with deionized ethanol and water six times. The final product was dried for 12 h at 60 °C.

Fabrication of TiO_2@RGO Hybrid DSSCs. The DSSC fabrication was performed as previously reported.[49,50] In brief, a TiO_2 thin-film electrode was prepared by spreading the uniform TiO_2 or TiO_2@RGO paste on fluorinated tin oxide glass (FTO-glass, Hartford Glass Co., 8Ω/sq, 80% transmittance in the visible spectrum) via a doctor blade technique. Uniform TiO_2 or TiO_2@RGO paste was made by addition of polyethylene glycol (PEG 20000, Fluka) aqueous solution (2 mL) to the synthesized TiO_2 or TiO_2@RGO powder (0.5 g) and grinded well by a mortar and pestle. Finally the prepared TiO_2 thin-film electrodes were annealed at 450 °C for 30 min in a static air furnace to remove the binder PEG. A dye solution consisting of 0.3 mM ruthenium 535 bis-TBA (N719, Solaronix) in ethanol (spectroscopy grade) was used for the dye loading of prepared TiO_2 electrode. For the dye loading process, TiO_2 electrodes were dipped in the dye solution at room temperature for 24 h under dark conditions, and then the dye-loaded TiO_2 electrodes were rinsed with ethanol and dried under a nitrogen stream. On the other hand, the electrode beam deposition was employed to coat a thin layer of Pt on the FTO glass and used as counter electrodes. The working and counter electrode were simply sealed with a 60 μm thick sealing surlyn sheet (SX 1170-60, Solaronix) at ∼70 °C. Through a small hole in the counter electrode, a redox electrolyte composed of 0.5 M LiI, 0.05 mM I_2, and 0.2 M *tert*-butyl pyridine in acetonitrile was injected into the cell, and finally the holes were sealed with a small piece of microscopic glass with surlyn sheet. The resulting DSSCs with active areas of ∼0.25 cm^2 were obtained.

Characterization and Measurements. Powder X-ray diffraction (XRD), scanning electron microscopy (SEM), transmission electron microscopy (TEM), and selected area electron diffraction (SAED) were utilized to characterize the titanium glycolate precursor and TiO_2@RGO samples. XRD was carried on a multipurpose high-performance X-ray diffractometer (PANalytical, Cu Kα radiation, λ = 1.5405 Å) in the 2θ range from 10° to 90° at a scanning rate of 0.03° s^{-1}. SEM images were performed on a field-emission electron microscope (ZEISS, SUPRA 40VP) operating at an acceleration voltage of 3 kV. TEM images and SAED patterns were recorded on a JEOL 2010 electron microscope at an accelerating voltage of 200 kV. The Raman spectrum of the as-synthesized product was carried out by a Raman microscope (Renishaw). Nitrogen adsorption was performed with Micromeritics ASAP 2020 (USA) to determine the Brunauer−Emmett−Teller (BET) specific surface area of the as-synthesized products. X-ray photoelectron spectroscopy (XPS) was carried out with an AXIS-NOVA CJ109 (Kratos Inc.) in the ranges of 0−800 eV to evaluate the surface compositions and interactions of the as-synthesized materials. An UV-2550 (Shimadzu) UV−vis spectrophotometer was used to measure the UV−vis diffuse reflectance spectrum of the prepared materials.

Photocurrent density−voltage (J−V) measurements were executed by the computerized digital multimeters (model 2000, Keithley) and a variable load under simulated sunlight illumination. A metal halide lamp (Phillips) of 1000 W power is the source of simulated sunlight. By using a Si photodetector fitted with a KG-5 filter (Schott) calibrated at NREL (USA) as a reference, the light intensity was set to global AM1.5 radiations at 100 mW/cm^2. This setup provided the actual solar efficiency without the need for correction because the spectral mismatch parameter for the dye cells was within 3% of unity. J−V measurements for all fabricated DSSCs were performed at room temperature.

3. RESULTS AND DISCUSSION

Morphology and Structure. The phase purity and crystal structure of the products obtained with different contents of graphene oxide after hydrothermal treatment were examined by powder X-ray diffraction (XRD) and compared to the results of pure TiO_2 (i.e., GT0). As shown in Figure 1, all of the diffraction peaks can be perfectly assigned to pure anatase TiO_2 (space group $I4_1/amd$, JCPDS Card No. 71-1167). No other diffraction peaks were detected, and the diffraction peaks were broadened, demonstrating the high purity and small particle size of TiO_2. The average crystal sizes of the as-prepared products were estimated from XRD line-broadening of anatase

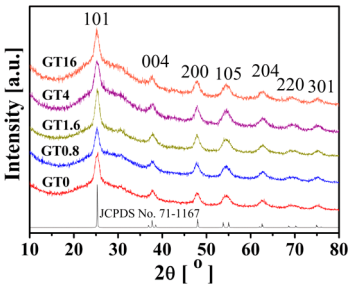

Figure 1. XRD patterns of the as-synthesized samples (GT0, GT0.8, GT1.6, GT4, and GT16).

at the (101) diffraction peak by employing the Scherrer equation. It was found that, with increasing the content of the reduced graphene oxide, the average crystal size of TiO_2 nanoparticles (shown in Table 1) decreases from 6.6 to 5.3 nm. Therefore, it can be proposed that the layered structure of reduced graphene oxide presents the significant surface for the nucleation of the TiO_2 nanoparticles.

The morphology and structure of the as-synthesized TiO_2 sample (GT0) without graphene oxide were further characterized by SEM, TEM, HRTEM, and SAED. As shown in Figure 2a–c, large-scale TiO_2 nanoparticles with diameters of less than 10 nm were obtained. The observed SAED pattern in Figure 2d shows the polycrystalline diffraction rings corresponding to the lattice planes of a TiO_2 anatase phase. Figure 2e shows a HRTEM image of the as-prepared TiO_2 nanoparticles. The clear lattice fringes of the side face of a single TiO_2 nanocrystal with a *d*-spacing of ~0.35 nm correspond to the (101) lattice plane, which also suggests that the TiO_2 nanoparticles were well-crystallized and had a high order of crystallinity. The insets in Figure 2e and Figure 2f show the Fourier transform (FFT) and inverse fast Fourier transform (IFFT) image of the selected area, respectively, where the diffraction pattern and lattice fringes are clearly seen.

Figure 3 shows the SEM and TEM images of the TiO_2@RGO hybrids (GT1.6) and bare GO, which demonstrate clear differences compared to GT0 (Figure 2). As seen in the inset of Figure 3a, with hydrothermal treatment of graphene oxide, two-dimensional wrinkled reduced graphene oxide sheets are obtained with a length of several micrometers. The SEM micrographs in Figure 3b and c show that the GT1.6 sample is composed of well-defined TiO_2@RGO nanostructures in which TiO_2 particles with small size uniformly diffuse and tightly attach with the RGO sheets, indicating that reduced graphene oxide could not only provide a large surface for the nucleation of TiO_2 nanoparticles but also inhibit their aggregation. As previously reported, through physisorption, electrostatic binding, or charge transfer interaction, TiO_2 nanoparticles could couple with RGO sheets, although Williams et al. employed the method of UV-assisted photocatalytic reduction of graphene oxide to prepare the TiO_2–RGO nanocomposites.[51] The HRTEM images shown in Figure 3d also reveal the well-defined crystallinity of TiO_2 nanoparticles with a lattice spacing of ~0.35 nm, which corresponds to anatase (101) planes. These observations demonstrate that good attachment of TiO_2 nanoparticles on the RGO was achieved via the above described two-step hydrothermal approach.

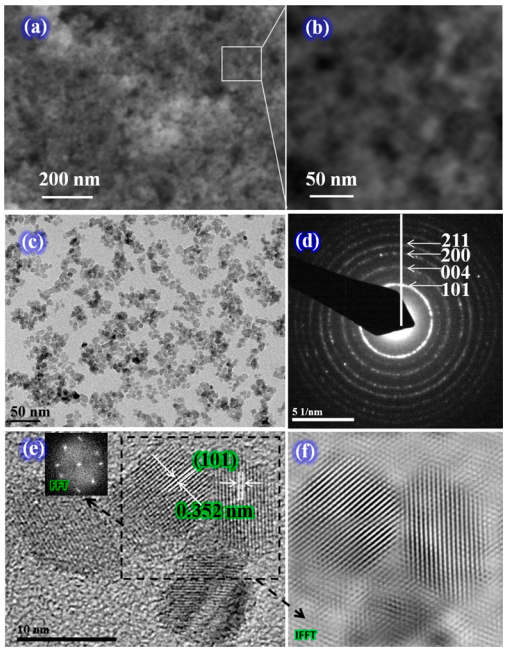

Figure 2. (a and b) SEM, (c) TEM, (e) HRTEM images, and the (d) SAED pattern of sample GT0. (Inset in e) FFT and (f) IFFT images of the selected area in (e).

XPS Analysis. Figure 4 displays the C 1s X-ray photoelectron spectroscopy (XPS) spectra of GO and the GT1.6 TiO_2@RGO hybrid. For graphene oxide (shown in Figure 4a), one typical peak located at ~284.6 eV originates from the graphitic sp^2 carbon atoms, and the other one at ~287.4 eV is attributed to carbon atoms bonding with oxygenate groups such as C–O.[52,53] The presence of oxygen-involving carbon in GO could provide active sites for directly connecting with the surface of TiO_2 nanoparticles. The C 1s XPS signal of the GT1.6 hybrids in Figure 4b shows binding energies at about 284.3, 285.1, and 288.4 eV. The main C 1s peak located at ~284.3 eV is assigned to elemental carbon, and the peak located at ~285.1 eV is due to defect-containing sp^2-hybridized

Table 1Physicochemical Properties of the As-Synthesized TiO_2 and TiO_2@RGO Hybrid Samples and the Short-Circuit Photocurrent Density (J_{SC}), Open-Circuit Voltage (V_{OC}), Fill Factor (F_F), and Conversion Efficiency (η) of Fabricated DSSCs

sample	graphene content (wt %)	crystallite size (nm)[a]	S_{BET} (m^2 g^{-1})	J_{SC} (mA cm^{-2})	V_{OC} (V)	FF (%)	η (%)
GT0	0	6.6	193.00	13.2	0.691	52.4	4.78
GT0.8	0.8	6.2	203.07	12.01	0.705	63	5.34
GT1.6	1.6	5.8	229.13	18.39	0.682	61.2	7.68
GT4	4	5.6	215.80	10.32	0.735	56	4.24
GT16	16	5.3	205.20	8.12	0.721	60.1	3.54

[a]Average crystal sizes were estimated from XRD line-broadening of the TiO_2(101) diffraction peak by employing the Scherrer equation: $D = K\lambda/(\Delta(2\theta)\cos\theta)$ where $\Delta(2\theta)$ is the line broadening at half the maximum intensity of the (101) diffraction peak of anatase, K is a coefficient with a typical value of 0.89, θ is the diffraction angle, and λ = 0.15405 nm (Cu Kα radiation) is the X-ray wavelength.

dx.doi.org/10.1021/am4013374 | ACS Appl. Mater. Interfaces 2013, 5, 6635–6642

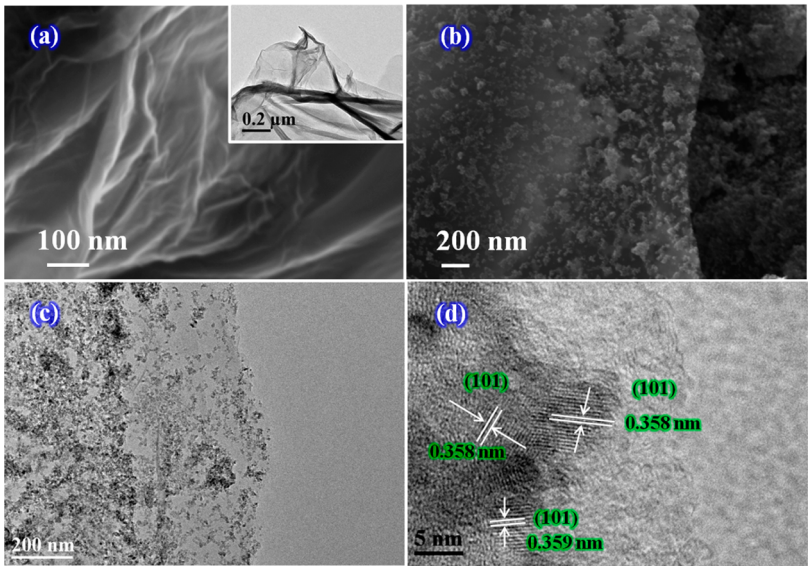

Figure 3. SEM images of (a) GO and (b) GT1.6 and (c) TEM and (d) HRTEM images of the GT 1.6 sample. Inset in (a) is a TEM image of reduced graphene oxide.

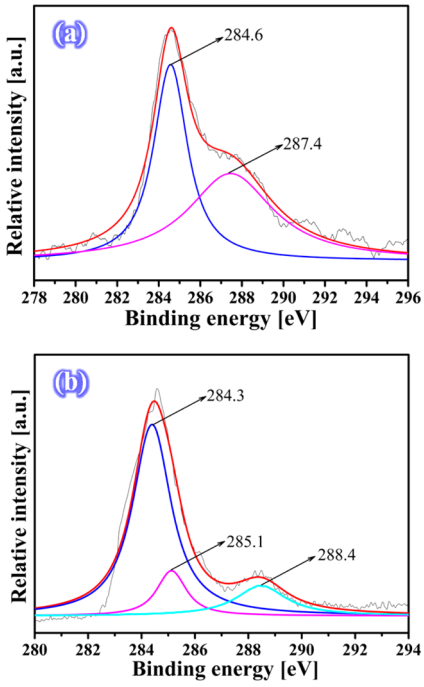

Figure 4. High-resolution XPS spectra of C 1s for (a) GO and (b) GT1.6.

carbons.[53] The relatively weak peak at ~288.4 eV is contributed to carboxyl carbon (O═C−O), which indicates that O═C−O−Ti bonds were formed, possibly by reaction of the −OH groups on the TiO_2 nanoparticles with the C−COOH groups on the GO surface through esterification.[53] By comparison, the peak at ~287.4 eV for the C−OH group on GO decreases remarkably or disappears in the C 1s XPS spectrum of the TiO_2@RGO hybrid, indicating that the introduced GO is efficiently reduced into RGO after hydrothermal treatment.

Raman Spectra and UV−Vis Diffuse Reflectance Spectroscopy. The typical structure of TiO_2@RGO hybrid (GT1.6) is studied comparing its Raman spectra with that of the pure TiO_2 (GT0 sample) and graphene oxide. As can be seen in Figure 5a, there are two typical peaks in the spectra of GO, namely, the D band at 1360 cm^{-1} and the G band at 1589 cm^{-1}.[54] In the case of pure TiO_2, several typical modes of the anatase phase including Eg(1), B1g(1), A1g + B1g(2), and Eg(2) are observed, corresponding to four characteristic bands at about 158, 397, 516, and 637 cm^{-1}, respectively.[53] For the TiO_2@RGO hybrid, the characteristic peaks of TiO_2 still exist along with the two typical peaks at ~1350 cm^{-1} (D band) and ~1585 cm^{-1} (G band), corresponding to the graphitic structures,[53,55] although the peak at ~158 cm^{-1} moves to ~179 cm^{-1}. Compared to the bands of GO, the D and G bands are slightly shifted to ~1350 and 1585 cm^{-1}, respectively, which assigns the value of pristine graphite (~1589 cm^{-1}), suggesting the transformation of TiO_2@RGO hybrids from GO and titanium precursors.[56−59] Upon the reduction of GO, Xiang et al. observed the D/G intensity ratio from TiO_2@RGO and C_3N_4@RGO composites increased in comparison to that of the GO spectra, indicating the decreasing of the average size of the in-plane sp^2 domains with reduction of GO and the existence of RGO sheets in the composite.[52,53] Herein, similar trends were observed for the formation of TiO_2@RGO hybrids, accompanying an increased D/G ratio, which indicates a decrease in the average size of sp^2 domains through the hydrothermal reductions. It is reasonable to propose that the reduction of GO causes it to fragment into new graphitic domains along the reactive sites, which led to RGO being smaller in size compared to GO before reduction.[54]

The interaction between TiO_2 and RGO in the fabricated hybrids was further investigated by UV−vis diffuse reflectance spectroscopy. As shown in Figure 5b, pure TiO_2 nanoparticles (GT0) show typical and intense absorption in the UV region (less than 380 nm), resulting from the electron transitions from the valence band (VB) to conduction band (CB). However, a broad background absorption in the visible light region was observed for the as-synthesized TiO_2@RGO samples, which could be ascribed to the existence of reduced graphene oxide in the TiO_2@RGO hybrids. Furthermore, with the introduction of RGO to TiO_2, the hybrids display a red shift of the absorption edge, which indicates the band gap of TiO_2@RGO hybrids has a tendency of narrowing. On the basis of the above results, it

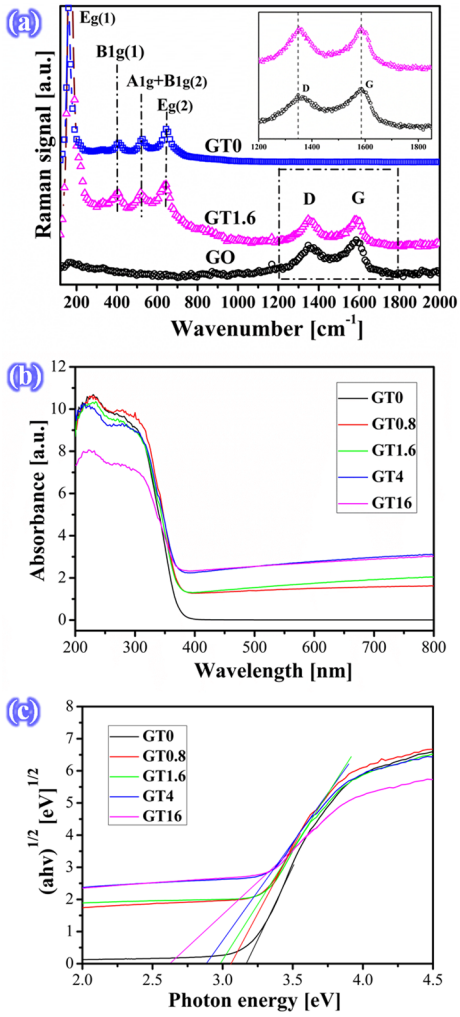

Figure 5. Raman spectra (a) of GO, GT1.6, and TiO_2. UV−vis diffuse reflectance spectra (b) of the as-synthesized TiO_2 nanoparticles and TiO_2@RGO hybrids. Plots of $(ahv)^{1/2}$ vs the photon energy (hv) for the as-synthesized TiO_2 and TiO_2@RGO hybrids (c).

was proposed that the Ti−O−C bond between TiO_2 and RGO was formed.[60] Similar phenomena were also observed for TiO_2−RGO composites prepared by Fan et al. confirming our proposal in this paper.[61] The band gap energies (E_g values) of TiO_2 and TiO_2@RGO samples could be calculated from a plot of $(\alpha h\nu)^{1/2}$ as a function of the energy of exciting light ($h\nu$).[62,63] An approximation of the band gap energies for different samples was obtained by taking the intercept of the tangent to the x-axis. As shown in Figure 5c, the band gap narrowing of all the TiO_2@RGO hybrids was clearly observed. Furthermore, the hybrids containing a higher concentration of the RGO show a narrower band gap, indicating that the interaction between TiO_2 nanoparticles and RGO sheets enhances with the concentration of RGO changing from 0.8% to 16%.[61] These results support that the preparation of TiO_2@RGO with such a hydrothermal process is successful.

Possible Formation Process. To understand the formation mechanism of the TiO_2@RGO hybrid, TiO_2 nanoparticles were firstly investigated in the present reaction system, which is based on in situ hydrolysis of titanium glycolate without any surfactants or other additives. The SEM and TEM images of the TiO_2 nanoparticles (Figures S2 and S3, Supporting Information) at different steps demonstrate that the reaction time has an important influence on the morphology of the final products. Scheme 1 illustrates the proposed mechanism in which nanoparticles are generated through a dissolution−recrystallization process of the preformed titanium glycolate particle precursors during hydrolysis. On the basis of the XRD patterns, the titanium glycolate precursor nanoparticles are amorphous in nature. However, with increasing of the reaction time for the reaction system under hydrothermal treatment, the structures of TiO_2 changed from nanoporous to nanoparticulate (Scheme 1(a)). We proposed that, as shown in step (2) in Scheme 1(b), during the process of hydrolysis, water could firstly penetrate into the outer surface and then go through into the inside of the precursor particles, which results in the formation of final TiO_2 nanoparticles with good dispersity. On the basis of the above results, the formation of the TiO_2@RGO hybrid (Scheme 1(c)) involves the same hydrolysis process of the titanium glycolate particles and reduction process of graphene oxide via hydrothermal treatment. The reaction systems are composed of the titanium glycolate presursor, graphene oxide, and water, which become homogeneous after the sonication treatment, in which titanium glycolate particles could attach to the surface of graphene oxide. Subsequently, TiO_2 nanoparticles formed on the RGO nanosheet through hydrothermal treatment. Figure S4 (Supporting Information) shows photographs of the reaction systems before and after hydrothermal treatment.

Dye-Sensitized Solar Cells (DSSCs). The as-prepared TiO_2@RGO hybrids were employed as the photoanode materials for the fabrication of DSSCs. The hybrid photoanodes with different RGO contents (0−16 wt %) were evaluated to investigate the impact of RGO on the performance of fabricated DSSCs. Figure S5 (Supporting Information) shows a photograph of a fabricated DSSC using GT1.6 as the photoanode material. The photocurrent density−voltage (J−V) characteristics of the DSSCs fabricated with the different TiO_2@RGO hybrid photoanodes are shown in Figure 6a and summarized in Table 1. The DSSC prepared with the hybrid GT1.6 photoanode exhibited the highest short-circuit photocurrent density (J_{SC}) of 18.3 mA cm^{-2} and the highest conversion efficiency of 7.68% with an open circuit voltage (V_{OC}) of 0.682 V and a fill factor (FF) of 61.2%. A lower conversion efficiency of 4.78% with a J_{SC} of 13.2 mA cm^{-2} was obtained from the DSSC fabricated with the GT0 photoanode. It is seen that the conversion efficiency increases after the addition of graphene, but the higher contents of graphene in the hybrid TiO_2@RGO materials result in a decreased conversion efficiency. The conversion efficiencies of the fabricated DSSCs with the GT0, GT0.8, GT1.6, GT4, and GT16 photoanodes are 4.78%, 5.34%, 7.68%, 4.24%, and 3.54%, respectively. Compared to the DSSC with the GT0 (pure TiO_2 nanoparticles) photoanode, the conversion efficiency and J_{SC} of the DSSC with GT1.6 are significantly improved by ~60% and ~38%, respectively. These improvements clearly demonstrate that a small content of RGO in the hybrid photoanode is sufficient to enhance the electron injection and electron transfer rate in the DSSC operation. The higher content of graphene in the TiO_2@RGO photoanodes may increase the resistance of the electrode and decrease the anodic reaction rate of the dye on the TiO_2 matrix, which may hinder the electron transportation upon illumination.[40] It was reported that the increment of J_{SC} resulted from the enhancement in amount of dye absorption through the photoanode, i.e., related to the high surface area of photoanode materials.[64] Nguyen et al. explained that the high surface area is

Scheme 1. (a) Illustration of the Preparation of Nanoparticulate TiO_2, (b) Possible Formation Process of TiO_2 Nanoparticles from the Titanium Glycolate Precursor,[a] and (c) Possible Formation Process of the TiO_2@RGO Hybrids

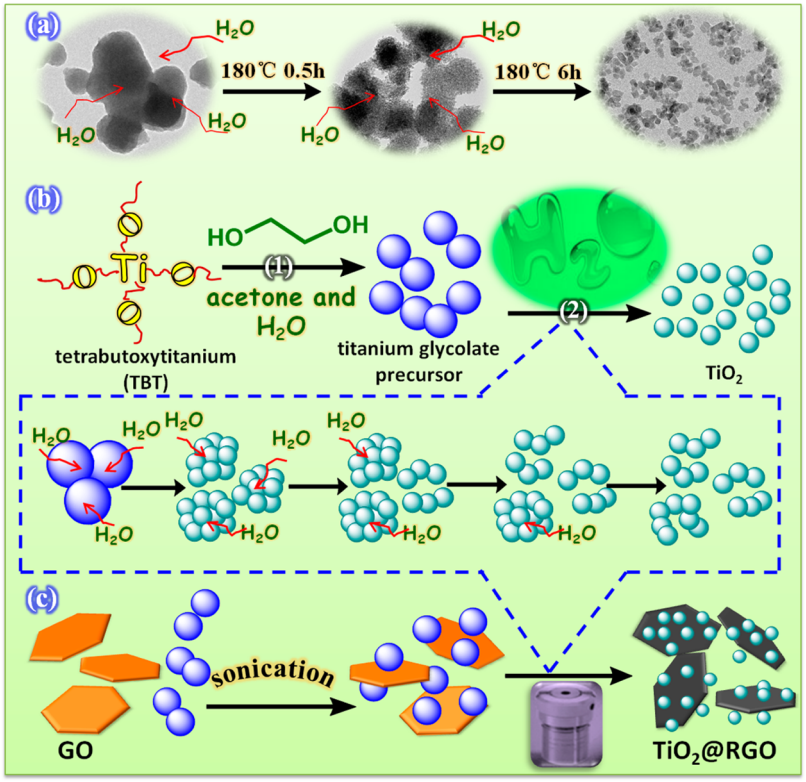

[a](1) Formation of titanium glycolate precursor by pouring the mixture of tetrabutoxytitanium and ethylene glycol into acetone and deionized water and (2) formation of TiO_2 nanoparticles in water from the titanium glycolate precursor via hydrothermal treatment: from nanoporous to nanoparticulate structures.

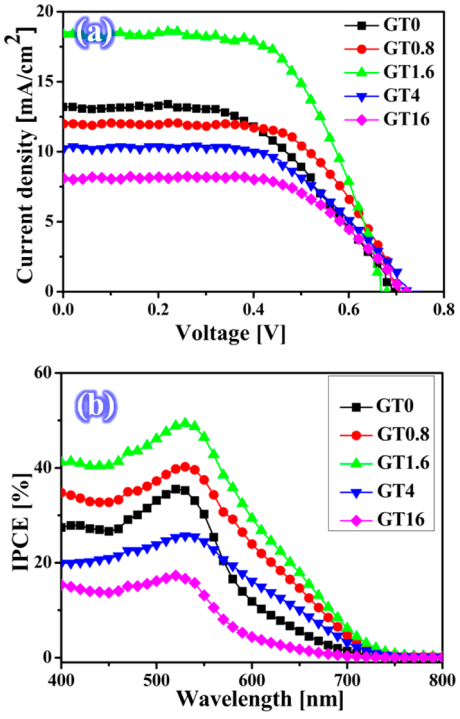

Figure 6. (a) J–V characteristics and (b) IPCE spectra of the five cells with different electrodes prepared with TiO_2@RGO with different amounts of reduced graphene oxide.

responsible for high dye loading but also the morphology and crystallinity of the materials.[65] From XRD and surface analysis, GT1.6 shows the improved crystallinity and highest surface area as compared to other compositions of hybrids. Therefore, the optimized GT1.6 hybrid photoanode delivers the highest PV performance with a high J_{SC} owing to its high electron injection and electron transfer rate because of the large surface areas of the GT1.6 photoanode.

To understand the different photocurrent characteristics of DSSCs fabricated with TiO_2@RGO hybrid photoanodes, the incident photon-to-current conversion efficiency (IPCE) spectra as a function of wavelength from 400 to 800 nm were collected. Figure 6b shows the IPCE measurements of DSSCs fabricated with hybrid TiO_2@RGO photoanodes. In general, the generation of IPCE is explained by the light-harvesting efficiency of dyes, the efficiency of electron injection, and the efficiency of collecting photoinjected electrons at the FTO substrate. The fabricated DSSCs exhibited a maximum absorption peak at ~532 nm, which mainly originated from the light harvesting of the dyes adsorbed by the photoanode films upon light illumination. The DSSC fabricated with the GT1.6 photoanode had the highest IPCE vlaue of 49.5%, while the GT0 and other hybrid photoanodes (GT0.8, GT4, and GT16) showed lower IPCE values of 35.2%, 40.2%, 25.7%, and 17.3%, respectively. The enhanced IPCE value is ascribed to the higher specific surface areas of the GT1.6 materials, which results in a considerably higher dye molecule loading and the ability to convert more photons to electrons.[66] In addition, the high IPCE of a DSSC also represents an improved electron transfer

dx.doi.org/10.1021/am4013374 | ACS Appl. Mater. Interfaces 2013, 5, 6635–6642

ability of the photoanode along with increased photocurrent density and photovoltaic performance.[67] On the other hand, the lower IPCE values in other DSSCs indicate that the electron-collection efficiency at the TiO_2/FTO substrate is poor due to the smaller surface area and lower dye absorption capacity of the materials. Thus, the high IPCE of the DSSC fabricated with the GT1.6 photoanode results in a high photocurrent density and photovoltaic performance.

4. CONCLUSION

In brief, a two-step hydrothermal method was developed to prepare TiO_2@reduced graphene oxide hybrids for solar cell applications. The prepared TiO_2@RGO hybrid photoanode material showed a much higher efficiency (7.68%) at a graphene content of 1.6 wt % in dye-sensitized solar cells than the efficiency of the pure TiO_2 (4.78%), demonstrating that the introduction of graphene accelerates the electron transfer and reduces the charge recombination. The present synthetic strategy is expected to provide a new approach for the preparation of TiO_2-involved hybrid materials such as TiO_2@carbon nanotubes and metal-ion-doped TiO_2 for solar energy conversion applications.

■ ASSOCIATED CONTENT

Ⓢ Supporting Information

Additional characterization data including XRD patterns, SEM and TEM images of titanium glycolate precursors, XRD patterns, SEM, TEM, and HRTEM images, and SAED patterns of sample GT0 at different reaction time, the photographs of reaction systems composited of the titanium glycolate presursor, graphene oxide, and water before and after hydrothermal treatment, and a photograph of a fabricated DSSCs using GT1.6 as the photoanode material. This material is available free of charge via the Internet at http://pubs.acs.org.

■ AUTHOR INFORMATION

Corresponding Author

*E-mail fjstadler@jbnu.ac.kr. Phone: +82-63-270-4039. Fax: +82-63-270-2306.

Notes

The authors declare no competing financial interest.

■ ACKNOWLEDGMENTS

This work was supported by a grant from the National Research Foundation of Korea (1201000936) and "Human Resource Development (Advanced track for Si-based solar cell materials and devices, project number: 20124030200080)" funded by the Korea government Ministry of Knowledge Economy and funds of Chonbuk National University (CBNU) in 2011. G Cheng acknowledges the China Scholarship Council (CSC, File No. 201208260002) for financial support. The authors would like to thank Mr. Jong-Gyun Kang (CBNU-CURF) for high-resolution TEM images. The authors would also like to thank the KBSI - Jeonju branch at CBNU for the BET, Raman, and XPS analyses. The help of Miss Jinyan Xiong for the UV−vis diffuse reflectance spectroscopy measurement is also appreciated.

■ REFERENCES

(1) Novoselov, K. S.; Geim, A. K.; Morozov, S. V.; Jiang, D.; Zhang, Y.; Dubonos, S. V.; Grigorieva, I. V.; Firsov, A. A. *Science* **2004**, *306*, 666−669.
(2) Stankovich, S.; Dikin, D. A.; Dommett, G. H.; Kohlhaas, K. M.; Zimney, E. J.; Stach, E. A.; Piner, R. D.; Nguyen, S. T.; Ruoff, R. S. *Nature* **2006**, *442*, 282−286.
(3) Huang, X.; Qi, X.; Boey, F.; Zhang, H. *Chem. Soc. Rev.* **2012**, *41*, 666−686.
(4) Sun, Y.; Wu, Q.; Shi, G. *Energy Environ. Sci.* **2011**, *4*, 1113−1132.
(5) Bajpai, R.; Roy, S.; Kumar, P.; Bajpai, P.; Kulshrestha, N.; Rafiee, J.; Koratkar, N.; Misra, D. S. *ACS Appl. Mater. Interfaces* **2011**, *3*, 3884−3889.
(6) Wang, H.; Cui, L.-F.; Yang, Y.; Sanchez Casalongue, H.; Robinson, J. T.; Liang, Y.; Cui, Y.; Dai, H. *J. Am. Chem. Soc.* **2010**, *132*, 13978−13980.
(7) Qiu, J.; Zhang, P.; Ling, M.; Li, S.; Liu, P.; Zhao, H.; Zhang, S. *ACS Appl. Mater. Interfaces* **2012**, *4*, 3636−3642.
(8) Wan, X.; Long, G.; Huang, L.; Chen, Y. *Adv. Mater.* **2011**, *23*, 5342−5358.
(9) Bonaccorso, F.; Sun, Z.; Hasan, T.; Ferrari, A. C. *Nat. Photonics* **2010**, *4*, 611−622.
(10) He, M.; Jung, J.; Qiu, F.; Lin, Z. *J. Mater. Chem.* **2012**, *22*, 24254−24264.
(11) Xiang, Q.; Yu, J.; Jaroniec, M. *Chem. Soc. Rev.* **2012**, *41*, 782−796.
(12) Li, Q.; Guo, B.; Yu, J.; Ran, J.; Zhang, B.; Yan, H.; Gong, J. R. *J. Am. Chem. Soc.* **2011**, *133*, 10878−10884.
(13) Peining, Z.; Nair, A. S.; Shengjie, P.; Shengyuan, Y.; Ramakrishna, S. *ACS Appl. Mater. Interfaces* **2012**, *4*, 581−585.
(14) Pan, X.; Zhao, Y.; Liu, S.; Korzeniewski, C. L.; Wang, S.; Fan, Z. *ACS Appl. Mater. Interfaces* **2012**, *4*, 3944−3950.
(15) Hou, C.; Zhang, Q.; Zhu, M.; Li, Y.; Wang, H. *Carbon* **2011**, *49*, 47−53.
(16) Lu, H.; Chen, Z.; Ma, C. *J. Mater. Chem.* **2012**, *22*, 16182−16190.
(17) Chen, H.; Müller, M. B.; Gilmore, K. J.; Wallace, G. G.; Li, D. *Adv. Mater.* **2008**, *20*, 3557−3561.
(18) Ravikumar; Scott, K. *Chem. Commun.* **2012**, *48*, 5584−5586.
(19) O'Regan, B.; Grätzel, M. *Nature* **1991**, *353*, 737−740.
(20) Hagfeldt, A.; Boschloo, G.; Sun, L.; Kloo, L.; Pettersson, H. *Chem. Rev.* **2010**, *110*, 6595−6663.
(21) van de Lagemaat, J.; Benkstein, K. D.; Frank, A. J. *J. Phys. Chem. B* **2001**, *105*, 12433−12436.
(22) Kopidakis, N.; Neale, N. R.; Zhu, K.; van de Lagemaat, J.; Frank, A. J. *Appl. Phys. Lett.* **2005**, *87*, 202106.
(23) Kongkanand, A.; Martínez Domínguez, R.; Kamat, P. V. *Nano Lett.* **2007**, *7*, 676−680.
(24) Kongkanand, A.; Kamat, P. V. *ACS Nano* **2007**, *1*, 13−21.
(25) van de Lagemaat, J.; Park, N. G.; Frank, A. J. *J. Phys. Chem. B* **2000**, *104*, 2044−2052.
(26) Tian, H.; Hu, L.; Zhang, C.; Mo, L.; Li, W.; Sheng, J.; Dai, S. *J. Mater. Chem.* **2012**, *22*, 9123−9130.
(27) Huang, F.; Li, Q.; Thorogood, G. J.; Cheng, Y.-B.; Caruso, R. A. *J. Mater. Chem.* **2012**, *22*, 17128−17132.
(28) Du, J.; Qi, J.; Wang, D.; Tang, Z. *Energy Environ. Sci.* **2012**, *5*, 6914−6918.
(29) Chen, T.; Guai, G. H.; Gong, C.; Hu, W.; Zhu, J.; Yang, H.; Yan, Q.; Li, C. M. *Energy Environ. Sci.* **2012**, *5*, 6294−6298.
(30) Kakiage, K.; Tokutome, T.; Iwamoto, S.; Kyomen, T.; Hanaya, M. *Chem. Commun.* **2013**, *49*, 179−180.
(31) Yan, J.; Zhou, F. *J. Mater. Chem.* **2011**, *21*, 9406−9418.
(32) Mor, G. K.; Shankar, K.; Paulose, M.; Varghese, O. K.; Grimes, C. A. *Nano Lett.* **2005**, *6*, 215−218.
(33) Liu, Z.; Misra, M. *ACS Nano* **2010**, *4*, 2196−2200.
(34) Sun, Z.; Kim, J. H.; Zhao, Y.; Bijarbooneh, F.; Malgras, V.; Dou, S. X. *J. Mater. Chem.* **2012**, *22*, 11711−11719.
(35) Wang, J.; Lin, Z. *Chem.–Asian J.* **2012**, *7*, 2754−2762.
(36) Muduli, S.; Lee, W.; Dhas, V.; Mujawar, S.; Dubey, M.; Vijayamohanan, K.; Han, S.-H.; Ogale, S. *ACS Appl. Mater. Interfaces* **2009**, *1*, 2030−2035.
(37) Yu, J.; Fan, J.; Cheng, B. *J. Power Sources* **2011**, *196*, 7891−7898.

(38) Jang, Y. H.; Xin, X.; Byun, M.; Jang, Y. J.; Lin, Z.; Kim, D. H. *Nano Lett.* **2011**, *12*, 479−485.
(39) Yang, N.; Zhai, J.; Wang, D.; Chen, Y.; Jiang, L. *ACS Nano* **2010**, *4*, 887−894.
(40) Tang, Y. B.; Lee, C. S.; Xu, J.; Liu, Z. T.; Chen, Z. H.; He, Z. B.; Cao, Y. L.; Yuan, G. D.; Song, H. S.; Chen, L. M.; Luo, L. B.; Cheng, H. M.; Zhang, W. J.; Bello, I.; Lee, S. T. *ACS Nano* **2010**, *4*, 3482−3488.
(41) He, Z.; Guai, G.; Liu, J.; Guo, C.; Loo, J. S.; Li, C. M.; Tan, T. T. *Nanoscale* **2011**, *3*, 4613−4616.
(42) Liu, X.; Pan, L.; Lv, T.; Zhu, G.; Lu, T.; Sun, Z.; Sun, C. *RSC Adv.* **2011**, *1*, 1245−1249.
(43) Anish Madhavan, A.; Kalluri, S.; K Chacko, D.; Arun, T. A.; Nagarajan, S.; Subramanian, K. R. V.; Sreekumaran Nair, A.; Nair, S. V.; Balakrishnan, A. *RSC Adv.* **2012**, *2*, 13032−13037.
(44) Jiang, X.; Herricks, T.; Xia, Y. *Adv. Mater.* **2003**, *15*, 1205−1209.
(45) Jiang, X.; Wang, Y.; Herricks, T.; Xia, Y. *J. Mater. Chem.* **2004**, *14*, 695−703.
(46) Xu, Y.; Bai, H.; Lu, G.; Li, C.; Shi, G. *J. Am. Chem. Soc.* **2008**, *130*, 5856−5857.
(47) Hummers, W. S.; Offeman, R. E. *J. Am. Chem. Soc.* **1958**, *80*, 1339−1339.
(48) Yan, Y.; Kuila, T.; Kim, N. H.; Ku, B.-C.; Lee, J. H. *J. Mater. Chem. A* **2013**, *1*, 5892−5901.
(49) Akhtar, M. S.; Khan, M. A.; Jeon, M. S.; Yang, O. B. *Electrochim. Acta* **2008**, *53*, 7869−7874.
(50) Akhtar, M. S.; Park, J.-G.; Kim, U.-Y.; Yang, O. B. *Mater. Chem. Phys.* **2011**, *127*, 479−483.
(51) Williams, G.; Seger, B.; Kamat, P. V. *ACS Nano* **2008**, *2*, 1487−1491.
(52) Xiang, Q.; Yu, J.; Jaroniec, M. *J. Phys. Chem. C* **2011**, *115*, 7355−7363.
(53) Xiang, Q.; Yu, J.; Jaroniec, M. *Nanoscale* **2011**, *3*, 3670−3678.
(54) Shen, J.; Yan, B.; Shi, M.; Ma, H.; Li, N.; Ye, M. *J. Mater. Chem.* **2011**, *21*, 3415−3421.
(55) Stankovich, S.; Dikin, D. A.; Piner, R. D.; Kohlhaas, K. A.; Kleinhammes, A.; Jia, Y.; Wu, Y.; Nguyen, S. T.; Ruoff, R. S. *Carbon* **2007**, *45*, 1558−1565.
(56) Ferrari, A. C.; Meyer, J. C.; Scardaci, V.; Casiraghi, C.; Lazzeri, M.; Mauri, F.; Piscanec, S.; Jiang, D.; Novoselov, K. S.; Roth, S.; Geim, A. K. *Phys. Rev. Lett.* **2006**, *97*, 187401.
(57) Basko, D. M.; Piscanec, S.; Ferrari, A. C. *Phys. Rev. B* **2009**, *80*, 165413.
(58) Bonaccorso, F.; Lombardo, A.; Hasan, T.; Sun, Z.; Colombo, L.; Ferrari, A. C. *Mater. Today* **2012**, *15*, 564−589.
(59) Lambert, T. N.; Chavez, C. A.; Hernandez-Sanchez, B.; Lu, P.; Bell, N. S.; Ambrosini, A.; Friedman, T.; Boyle, T. J.; Wheeler, D. R.; Huber, D. L. *J. Phys. Chem. C* **2009**, *113*, 19812−19823.
(60) Zhang, H.; Lv, X.; Li, Y.; Wang, Y.; Li, J. *ACS Nano* **2010**, *4*, 380−386.
(61) Fan, W.; Lai, Q.; Zhang, Q.; Wang, Y. *J. Phys. Chem. C* **2011**, *115*, 10694−10701.
(62) Abaker, M.; Umar, A.; Baskoutas, S.; Dar, G. N.; Zaidi, S. A.; Al-Sayari, S. A.; Al-Hajry, A.; Kim, S. H.; Hwang, S. W. *J. Phys. D: Appl. Phys.* **2011**, *44*, 425401.
(63) Abaker, M.; Umar, A.; Baskoutas, S.; Kim, S. H.; Hwang, S. W. *J. Phys. D: Appl. Phys.* **2011**, *44*, 155405.
(64) Benkstein, K. D.; Kopidakis, N.; van de Lagemaat, J.; Frank, A. J. *J. Phys. Chem. B* **2003**, *107*, 7759−7767.
(65) Nguyen, T.-V.; Lee, H.-C.; Yang, O. B. *Sol. Energy Mater. Sol. Cells* **2006**, *90*, 967−981.
(66) Wang, Q.; Moser, J.-E.; Grätzel, M. *J. Phys. Chem. B* **2005**, *109*, 14945−14953.
(67) Nazeeruddin, M. K.; Baranoff, E.; Grätzel, M. *Sol. Energy* **2011**, *85*, 1172−1178.